Coherent two-beam steering of delocalized nonlinear photoluminescence in a plasmon cavity

Florian Dell'ova, Diana Shakirova, Yoann Brûlé, Laureen Moreaud, Gérard Colas Des Francs, Erik Dujardin, Alexandre Bouhelier

Research Article | Vol. 30, No. 10 / 9 May 2022 / Optics Express 17517
Optics EXPRESS

Coherent two-beam steering of delocalized nonlinear photoluminescence in a plasmon cavity

FLORIAN DELL'OVA,[1] DIANA SHAKIROVA,[1,2] YOANN BRULÉ,[1] LAUREEN MOREAUD,[3] GÉRARD COLAS-DES-FRANCS,[1] ERIK DUJARDIN,[1,3] AND ALEXANDRE BOUHELIER[1,*]

[1]*Laboratoire Interdisciplinaire Carnot de Bourgogne, CNRS UMR 6303, Université de Bourgogne Franche-Comté, 9 Av. A. Savary, 21078 Dijon, France*
[2]*School of Physics and Engineering, ITMO University, Saint-Peterburg, 197101, Russia*
[3]*CEMES CNRS UPR 8011 and University of Toulouse, 29 rue J. Marvig, 31055 Toulouse, France*
[*]*alexandre.bouhelier@u-bourgogne.fr*

Abstract: We aim at controlling the spatial distribution of nonlinear photoluminescence in a shaped micrometer-size crystalline gold flake. Interestingly, the underlying surface plasmon modal landscape sustained by this mesoscopic structure can be advantageously used to generate nonlinear photoluminescence (nPL) in remote locations away from the excitation spot. By controlling the modal pattern, we show that the delocalized nonlinear photoluminescence intensity can be redistributed spatially. This is first accomplished by changing the polarization orientation of the pulsed laser excitation in order to select a subset of available surface plasmon modes within a continuum. We then propose a second approach to redistribute the nPL within the structure by implementing a phase control of the plasmon interference pattern arising from a coherent two-beam excitation. Control and engineering of the nonlinear photoluminescence spatial extension is a prerequisite for deploying the next generation of plasmonic-enabled integrated devices relying on hot carriers.

1. Introduction

Noble metals are known to generate nonlinear photoluminescence (nPL) upon near-infrared pulsed laser irradiation [1]. nPL is spectrally characterized by its broad-band distribution spanning the visible wavelength region. The continuum is generally bounded by the interband absorption edge of the material in the short wavelength range (about 550 nm for Au) and by the laser line in the long wavelength limit (typically 800 nm for femto-second Ti:Saph lasers). It has been shown that both the yield and the spectral shape of the nPL can be significantly modified by exciting local surface plasmon resonances supported by small metal objects. For instance, the detected nPL intensity can be greatly enhanced when the laser wavelength matches the resonant absorption of a nanoparticle [2,3], and its emission spectrum reflects the underlying local density of optical states in the covered spectral range [4,5].

Mechanisms at the origin of this nPL generation are still debated. For Au nanostructures, the process was understood as a radiative recombination of multiphoton absorption events promoting low-lying electrons of the *d*-band to unoccupied states in the *sp*-band [1,6,7]. This hypothesis has been recently challenged by consistent reports of large non-integer nonlinearity orders [8–10] that are difficult to conciliate with a sequential photon absorption between electronic bands. Furthermore, nPL was also observed with other metals [11–13] and seems to be a generic attribute of nano-sized metallic objects. Alternative emission mechanisms were then proposed to account for these new observations including resonant electronic scattering [14,15] and intraband spontaneous emission [16,17]. All these assumptions rely on a common process involving the

#456599 https://doi.org/10.1364/OE.456599
Journal © 2022 Received 18 Feb 2022; revised 31 Mar 2022; accepted 12 Apr 2022; published 6 May 2022

Optics EXPRESS

decay of an out-of-equilibrium electron gas swiftly formed after the absorption of the laser pulse [18].

In parallel of this on-going scientific debate, the properties of the nPL have been advantageously exploited. For instance, nPL can be used to sensitively probe the local electric field [19–21] or serve as a contrast agent in bio-imaging [22–24]. Another nPL captivating facet is the delocalization of nPL in mesoscopic geometries. The nonlinear response is not necessarily spatially restrained to the illumination location but may explore the full expanse of a given structure. This has been demonstrated for instance with metal nanowires [25–28] and two-dimensional Au crystal flakes [29,30]. The underpinning delocalization channel is the excitation and propagation of surface plasmon polaritons (SPP) transporting the optical energy according to the supported plasmonic modal landscape.

This causal relationship between the nPL and surface plasmon modes offers a unique gateway to tailor the spatial extent of the nonlinear response in complex geometries. Indeed, the SPP modal distribution can be readily adjusted by modifying the shape and the size of two-dimensional plasmonic objects [31–34]. Furthermore, eigen modes can be selectively excited to redistribute the local electric field. This is performed either by adjusting the position of excitation onto the structure [29,35,36], or by changing the polarization of the incident field [37–39]. An additional degree of control is brought by implementing coherent responses and phase shaping of incoming pulses [21,40–42].

Inspired by the diversity of strategies deployed to harness a modal landscape, we combine in this report different means to control the SPP modes populating a two-dimensional Au crystalline cavity. Our motivation is to reconfigure by-design the nonlinear photoluminescence spatial distribution and introduce some agility in a device. This is a crucial aspect required to push forward the development of plasmonic-enabled computational tasks [29] or hot-carriers reactors [27,43].

2. Descriptions of the sample and of the experimental setup

Our starting strategy to control the surface plasmon polariton modes is to design a well-defined two-dimensional object. In this study, it is a micrometer-sized double hexagon (DH) Au crystalline cavity. Quasi two-dimensional Au crystals offer a high performance platform for designing plasmonic devices [32,44–46]. Our choice for this particular geometry is dictated by several aspects. First, the lateral dimensions of the structure offer a continuum of SPP modes that can be mobilized simultaneously because they either overlap spatially or spectrally. Second, a DH offers a large number of apexes (10) and edges (10), which are all potential entry points for exciting SPPs. Finally, the rotational and mirror symmetries typical for this shape simplify the complexity of the mode pattern. Figure 1(a) is a colorized scanning electron microscope image of the double hexagon used in this work. The edges of the DH cavity are 715 nm long. Large crystalline Au flakes are grown by reduction of gold chloride in the presence of ethyleneglycol and aniline according to an established protocol [47]. The Au flakes come with lateral sizes comprised between 1 and 10 μm and thickness between 30 and 60 nm. The flakes are constituted of two ultrathin single crystals separated by a single twin and exposing atomically smooth (111) basal planes. The colloidal dispersion is drop-casted onto a glass coverslip coated with 10 nm of conductive Indium Tin Oxyde. The structure is carved by focused-ion beam milling in 6-10 micron wide Au flakes as described in Refs. [29,48]. The DH shown in Fig. 1(a) is milled in an 35-nm thick Au flake as measured by atomic force microscopy.

We numerically interrogate the plasmonic response of the gold DH by considering the surface plasmon local density of states (SP-LDOS) [32]. SP-LDOS along a given direction $i = x, y$ or z is computed at positions $\mathbf{r}$ within the metallic structure as

$$\rho_i(\mathbf{r}, \omega_0) = \frac{1}{\pi\omega_0^2}\mathrm{Im}\left[S_{ii}(\mathbf{r}, \mathbf{r}, \omega_0)\right] \quad (1)$$

Optics EXPRESS

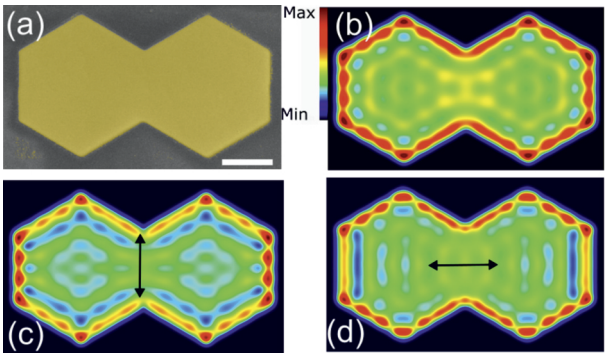

Fig. 1. (a) Colorized scanning electron microscope (SEM) image of a double hexagon carved from Au crystalline flake. The scale bar is 500 nm. (b) Total in-plane surface plasmon local density of state (SP-LDOS) calculated at 810 nm. (c) and (d) are projected SP-LDOS along the two main directions indicated by the double arrows.

where S_{ii} is the ith diagonal component of the Green's tensor $\mathbf{S}$. The in-plane SP-LDOS is $\rho_{\parallel} = (\rho_x + \rho_y)/2$. The continuum of SPP modes interacts to form a complex two-dimensional in-plane SP-LDOS as shown in Fig. 1(b) for an excitation wavelength of 810 nm. As anticipated above, the periphery of the DH concentrates the largest density of SPP modes and is therefore optimally suited for optically coupling-in an external laser illumination because of the additional momenta created by diffraction of the focused laser at the physical edge. The SP-LDOS is a vectorial quantity; its value at specific locations of the double hexagon changes with the projection direction. To illustrate this point, we show in Fig. 1(c) and (d) in-plane SP-LDOS calculated along the components indicated by the double arrow. While the amplitude at the vertices remains high for the two cases, the SP-LDOS at the edges differs: the quantity is maximized when an edge is aligned with the projection.

For the experimental part, the double hexagon is excited by a near infra-red Ti:Sapphire 140 femtosecond pulsed laser tuned at $\lambda_0 = 810$ nm and cadenced at $f_{\text{rep}} = 80$ MHz. The laser is focused onto a diffraction-limited area (beam waist ~ 270 nm) on the object by a high numerical aperture (NA) objective lens (NA = 1.49) as sketched in Fig. 2(a). The combination of an ultrafast pulsed laser and a tight focusing enables the emergence of nonlinear responses from the constituting material. The experimental setup can be conveniently split in two parts separating excitation and collection paths. For the excitation path, we control the orientation of the linear polarization delivered by the laser with a half-wave plate. We introduce the possibility to produce a pulse replica by splitting the laser into two arms in order to switch, at will, from a single- to a double-beam irradiation. Exciting a second entry point brings some agility by recruiting a higher number of interacting modes. The polarization of each pulse can be independently adjusted and a delay stage implemented on one arm enables to synchronize the arrival time of the pulses at the sample. Together with the shaping of the structure, the control of the polarization and the relative time (phase) delay between the two pulses impinging on the DH complete our strategy for configuring the nPL spatial distribution.

The upconverted signal produced by the DH at shorter wavelength than the laser line is captured by the same objective. A dichroic beam splitter with a short-pass cutoff at 700 nm rejects the laser line from the detection. The second-harmonic generated by the sample is also spectrally filtered out. This upconverted signal is identified in this work as a nonlinear photoluminescence emitted by structure. Details about the nonlinearity of the response can be found in [13]. Here, we implement two imaging modalities for assessing the nPL contribution. A confocal imaging mode is used to investigate the efficiency of nPL generation at the location of the excitation spot

Optics EXPRESS

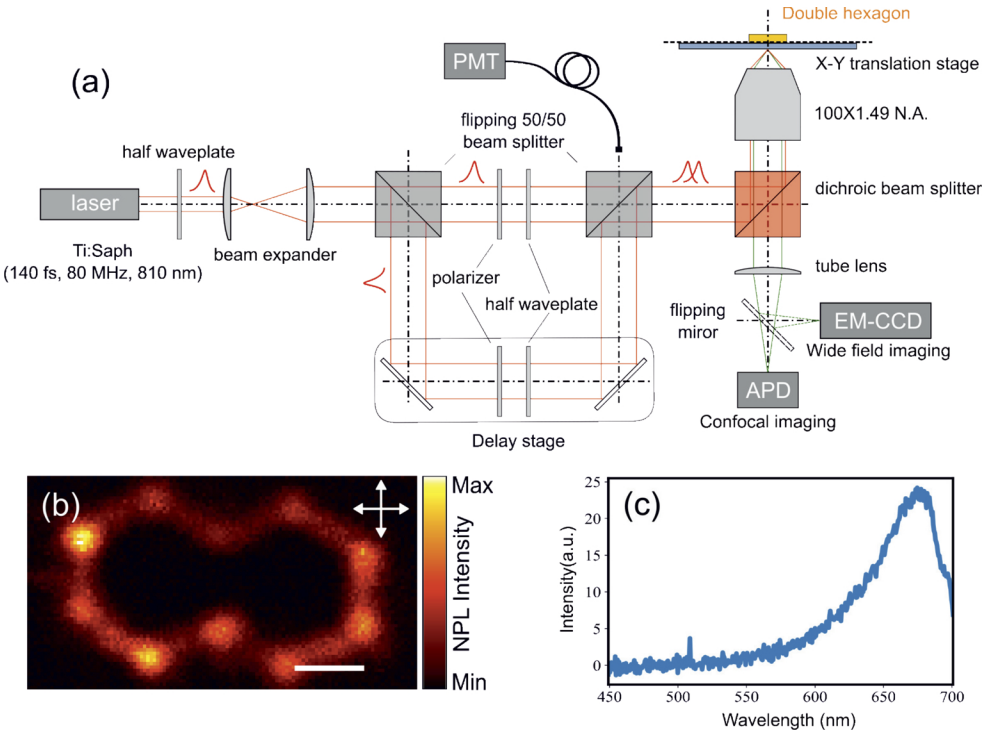

Fig. 2. (a) Sketch of the experimental setup. The excitation can be split into two arms to opt for a single-beam or a double-beam excitation. A delay stage controls the timing of the pulses. One of the beam has a fixed position in the focal plane while the second can be steered (not shown). nPL is detected either in a confocal imaging mode or in wide-field configuration. (b) nPL intensity map constructed by summing two confocal images taken with orthogonal polarizations. Scale bare is 500 nm. (c) Typical nPL spectrum emitted by the DH showing a decaying tail in the visible spectral region. The abrupt drop after 680 nm reflects the cutoff wavelength of the dichroic beam splitter.

by laterally scanning the DH with a piezo-electric stage. The nPL is detected by an avalanche photo-diode counting module (APD) for each (x, y) position of the scanning stage. An image can then be readily constructed as depicted in Fig. 2(b). The figure represents the sum of two confocal nPL maps obtained independently for two orthogonal polarization orientations materialized by the double arrows. The average laser intensity is 1 MW·cm^{-2}. We unambiguously observe a strong nPL response along the perimeter of the DH cavity with hot spots located at the apexes.

The nPL intensity has been empirically linked previously to the square of the SPLDOS convoluted with the point-spread function of the microscope [32]. Regions of high SP-LDOS highlighted in Fig. 1(b) are indeed overlapping with the locations providing the highest nPL intensities detected in the reconstructed confocal map. The amplitude of the nPL signal may also be locally dependent on the intricacy of the band structure at the edges [30]. The strength of the nonlinear signal when the focus is located in the interior of the structure is orders of magnitude weaker. This is probably due to a combination of factors including inefficient surface plasmon excitation by in-plane incident wavevectors contained with the NA of the objective and low surface roughness of the crystalline flake. Figure 2(c) is a spectrum taken when focusing one laser beam at one apex of the DH. Since the DH accommodates a continuum of SPP modes overlapping spectrally and spatially, no particular resonances are contributing to re-shape the emitted spectrum. The spectrum reflects the standard decaying tail of the nPL [13]. The

Optics EXPRESS

congruence between the spectra investigated in depth in Ref. [13] on similar objects and the one presented in Fig. 2(c) helps us to identify the origin of the nPL as the thermal signature of a hot electron gas relaxing radiatively by colliding with the side wall of the object.

The confocal maps do not provide the full information about the lateral extension of the nPL response inside the DH for a given excitation point. To measure where the nPL is emitted and how it is distributed in the structure we operate a second imaging modality by using an electron multiplying charge coupled device (EM-CCD) to record wide-field nPL images. Wide-field imaging is the default mode for all the experimental images presented hereafter.

3. Single beam excitation : polarization control of the delocalized nPL

We first investigate the effect of the orientation of the incident polarization on the routing of the nPL spatial extension throughout the device in a single-beam configuration. The objective is to mobilize a polarization-selected set of SPP modes within the available continuum to adequately redistribute the nPL.

Figure 3(a) shows a nPL wide field image when the focal spot overlaps the bottom left corner of the cavity. This excitation area is denoted by the black circle labelled I_1. This apex, like all other, holds a large SP-LDOS regardless of the incident polarization promoting an efficient coupling to the SP modes (see Fig. 1). Note that other apexes may as well serve as alternative entry points. The orientation of the polarization is horizontal (double arrow). The image is acquired with an integration time of $\tau = 1$ s and is background corrected. The wide-field image unambiguously shows that the nPL emission is not restricted to the excitation area but is spatially extended throughout the double hexagon. This information is completely hidden in confocal maps. The wide-field map reveals that the nPL signal is mostly emitted from the edges and vanishes within the structure. Two effects are contributing to produce the nPL emission at the periphery. First, SPP excited and propagating from I_1 at λ_0 are interacting with the physical edges of the DH by being reflected back inside the DH or scattered out to free-propagating photons. The reflection of the SPP at the edges is at the origin of the SP-LDOS oscillatory pattern displayed in Fig. 1(b). The interaction with the contour is typically associated to a local enhancement of the electromagnetic field and consequently a rise of nPL [26]. Assuming that nPL reflects the radiative fate of a hot electron gas [13,17], the emission of a photon must be triggered by a momentum exchange [49]. In this case, this exchange is promoted by hot carriers colliding with the sidewall of the object. Hence, the amplitude of the nPL signal at a given point of the perimeter is primarily dictated by the underlying strength of the plasmonic field at the considered location.

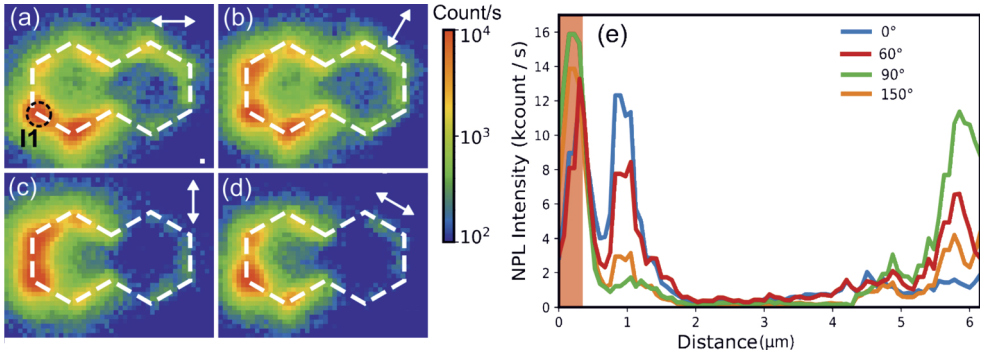

Fig. 3. (a) to (d) Wide field nPL maps of a single beam excitation of the cavity with 0°, 60°, 90° and 150° polarization orientations when the laser spot is fixed at I_1 (circle in (a)). The color scale is in logarithmic units to visualize the weakest regions. (e) Profiles taken along the entire contour

Optics EXPRESS

Figure 3(b) to (d) are three nPL wide-field images taken with different polarization orientations of 60°, 90° and 150°, respectively. The excitation point remains the same at I_1. One can clearly observe a spatial redistribution of nPL intensity depending on the polarization. For instance, nPL is emitted from all corners and edges of the structure at 0° and 150° orientations, whereas the signal remains mostly confined on the left-hand side hexagon for 60° and 90° with a weak excursion on the right side at selected edges. The different levels of nPL intensity detected along the contour of the structure are shown in Fig. 3(e) for the set of polarization orientations. The plots start at the excitation spot (highlighted in red) and follow counterclockwise the inner part of the entire perimeter. The graph clearly demonstrates a fine polarization tuning of the nPL signal. The largest variations are observed nearby the excitation spot (start and end of the axis 'Distance') where SPP propagation losses are minimal. For instance, the blue curve (0°) features an opposite evolution to the green curve (90°). The region with comparatively low nPL intensities corresponds to the perimeter of the right hexagon. There, SPPs launched at I_1 are attenuated by intrinsic losses and nPL is naturally weaker. Nonetheless, the sensitivity of the nPL spatial distribution to the polarization orientation provides a first handle to adjust the strength of a nonlinear process in remote areas of an object. This mechanism can be deployed for instance to reconfigure a Boolean readout level [48].

Figure 4 helps us at understanding why the polarization is redistributing the nPL in the double hexagon. We show two computed near-field intensity maps of the surface plasmon field developing within the object for two orthogonal orientations of the polarization. The simulated focal spot takes into account the experimental parameters (N.A) and overlaps the same apex I_1 as in Fig. 3. Clearly, the polarization is greatly affecting the spatial arrangement of the total surface plasmon field by selecting modes featuring a non-zero projection along the incident electric field. At that stage, we are not able to formally link the computed intensity maps of Fig. 4 with the experimental nPL snapshots displayed in Fig. 3. However, the general trend seems to be preserved: the SPP field and by consequence the nPL is present at the edges of the right hand side hexagon for a horizontal polarization (Fig. 3(a) and Fig. 4(a)), but are both vanishing for the orthogonal orientation.

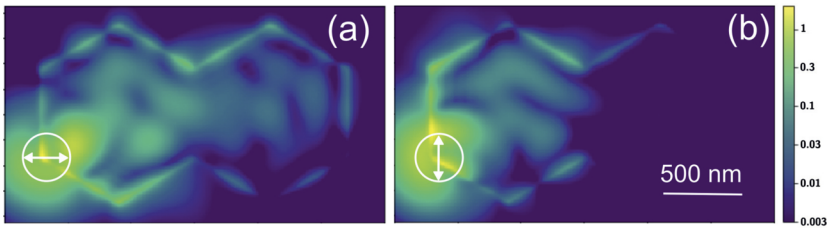

Fig. 4. (a) and (b) are normalized calculated near-field intensity maps of the surface plasmon field developing in the structure at the laser wavelength for two orthogonal polarizations indicated by the double arrow. The double hexagon is excited at I_1 mimicking the condition discussed in Fig. 3. The focal field is fully taken into account in these calculations. Logarithmic color scale.

4. Two-beam excitation : phase control of the delocalized nPL

The double hexagon cavity has a mesoscopic size that can sustain multiple excitation inputs. Therefore, it provides a unique gateway for the coherent exploration of the tailored plasmonic modal landscape using two simultaneous entry points. This additional level of control has been identified as a requisite to experimentally implement complex Boolean functions and arithmetic operations [48]. To this aim, we produce a pulse replica and synchronize the arrival time of both pulses at the sample with the delay stage shown in Fig. 2(a). The phase difference $\Delta\phi$ between

Optics EXPRESS

the two laser pulses can be finely adjusted by scanning the delay stage around the optical contact point. Adjusting the phase is an essential element for coherently controlling the interaction between SPPs launched by both beams. We monitor the phase difference with a photo-multiplier tube (PMT) aligned on a bright fringe of the interference pattern generated by the two collimated laser beams exciting the recombining beam-splitter (Fig. 2(a)). Since the interference fringes are laterally shifted when the delay stage moves, monitoring the voltage delivered by the PMT gives access to the phase difference.

The methodology for adjusting and measuring the phase difference is illustrated in Fig. 5(a) showing the evolution of the PMT voltage output when the delay τ between the two pulses is scanned. To maximize the visibility, the two laser spots are here focused at the same location of the DH and hold the same polarization. The nPL intensity simultaneously recorded by the APD is displayed in Fig. 5(b) where two distinct regimes can be identified.

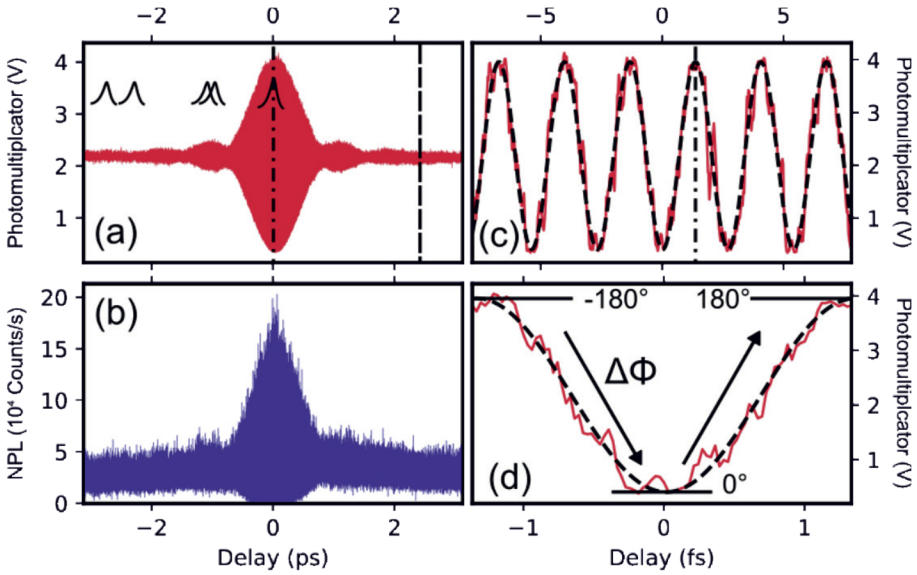

Fig. 5. (a) PMT output recorded while the delay stage is scanned over 6 ps and the two laser spots are focused on the cavity. The pictograms represent the temporal overlap between the two pulses. The maximum contrast corresponds to the optical contact of the two pulses and defines the relative delay $\tau = 0$. (b) nPL intensity simultaneously acquired by the APD. (c) Temporal zoom around $\tau = 0$ highlighting the coherent modulation between the two pulses. The black dotted line is a fit using the pulsation of the laser. (d) One-period extract showing the conversion from the PMT output voltage to the relative phase.

First, an incoherent excitation regime is observed when the two laser pulses are temporally well separated ($|\tau|>1.5$ ps). This corresponds to a constant PMT voltage proportional to the average intensity of the two collimated beams exciting the beam-splitter (*i.e.* no interference fringes). In this excitation regime the total nPL intensity reflects the time-averaged incoherent summation of the nPL produced by each individual pulses and is thus independent on the delay.

The second regime corresponds to a time delay enabling a temporal overlap of the two pulses (-1.5 ps$<\tau<1.5$ ps). The two pulses are coherently interacting and an interference pattern builds up at the exit of the beam-splitter. The optical contact between the two pulses is readily identified on the PMT output when the interference contrast is maximal and arbitrarily sets the origin of the relative delay $\tau = 0$. In Fig. 5(c), we show a 15 fs delay frame taken around $\tau = 0$ highlighting intrapulse modulations. The oscillations are due to constructive and destructive interferences set by the phase difference between the two laser pulses. The period of the oscillation is determined

Optics EXPRESS

by a simple sinusoidal fit (black dashed line) and corresponds to the laser pulsation $\omega_0 = 2\pi c/\lambda_0$. Each time the delay stage is moved by λ_0, the relative phase is shifted by 360° and corresponds to one period of the PMT signal. The absolute value of the phase difference $\Delta\phi$ between the two pulses is deduced from the PMT output voltage and its sign from the one of the slope. This is depicted in Fig. 5(d) for the central period where the voltage given by the PMT is converted in a relative phase varying between -180° and 180°. The interferogram and consequently the phase conversion exemplified in Fig. 5 will be modified if the excitation areas are spatially separated on the DH or if the polarization of the beams are changed. Hence, the voltage-to-$\Delta\phi$ conversion abacus needs to be re-determined every time the excitation conditions are modified.

With this experimental calibration protocol we are able to associate a relative phase value to each wide field nPL image acquired at different delays. Figures 6(a) to (c) show wide-field nPL images taken with a relative phase of $\Delta\phi = -2°$, 98° and 175°, respectively, when the two excitation spots are focused on locations marked I_1 and I_2. The beams hold the same polarization direction indicated by the double arrow in Fig. 6(a). Several SP modes are excited coherently in the cavity by each of the two laser beams, depending on their respective position, polarization and phase. Only the latter is changed during this experiment, and we clearly observe a redistribution of the nPL intensity in the cavity for the different $\Delta\phi$ displayed. Let us consider for instance the area materialized by the white square labelled O_1. A weak nPL signal is emitted for $\Delta\phi = -2°$, but the signal gets stronger with increasing phase difference. The square labelled O_2 features the opposite behavior: the nPL signal is strong at $\Delta\phi = -2°$ and vanishes at $\Delta\phi = 175°$. The nPL signal strengths of these two areas can be finely tuned by a control of the phase difference between the two excitation beams. This is demonstrated in Fig. 6(d) whereby the level of the nPL signals can be adjusted over an order of magnitude by controlling the coherent superposition of SP modes. What is demonstrated here for two excitation locations can be applied to all other meaningful vertices and edges of the object and polarization states. As an illustration of the reconfiguration agility brought by the phase, we show in Fig. 7 a series of near-field maps computed at the laser wavelength for the entry nodes I_1 and I_2 with incident polarizations 30° and 70° respectively. Each frame is calculated for a varying phase difference $\Delta\phi$ between the field incident on I_1 and I_2. As expected, the phase influences the interferogram of interacting surfaces plasmons, and drastic variations can be readily observed on the contour of the object, including near the O_2 region considered previously.

Optics EXPRESS

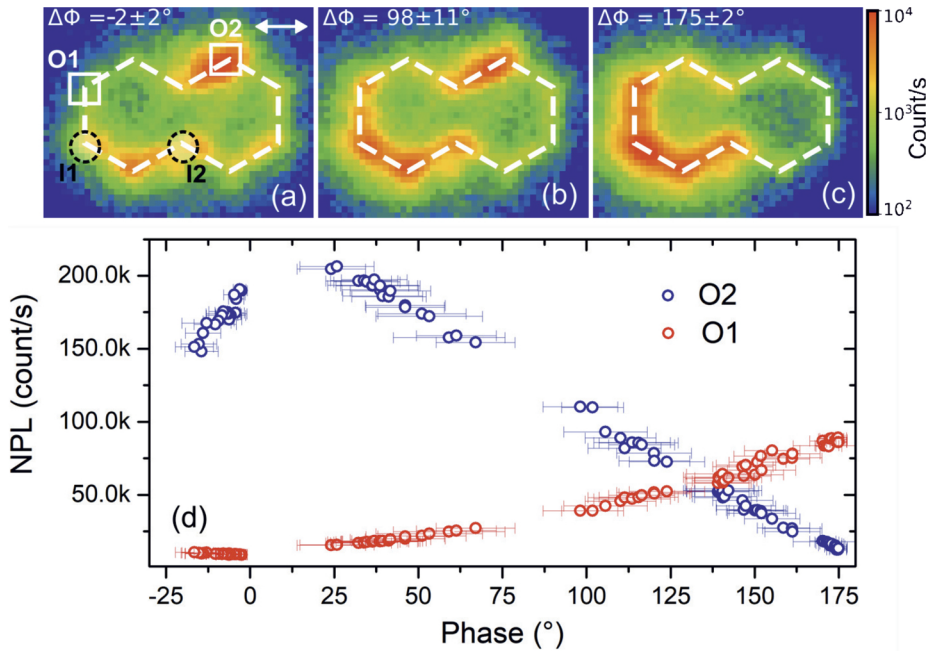

Fig. 6. (a) to (c) Wide-field nPL images recorded with a relative phase of -2°, 98° and 175°, respectively. For each record, excitation locations I_1 and I_2 (white circles in (a)) are kept fixed with a horizontal polarization (white arrow). (d) Relative phase dependence of the nPL intensity emitted by the locations O_1 and O_2 (white square in (a)). The nPL signal is summed on a 0.14 μm^2 detection area. The error bars are estimated from the variation of the PMT signal occurring during the measurement integration time.

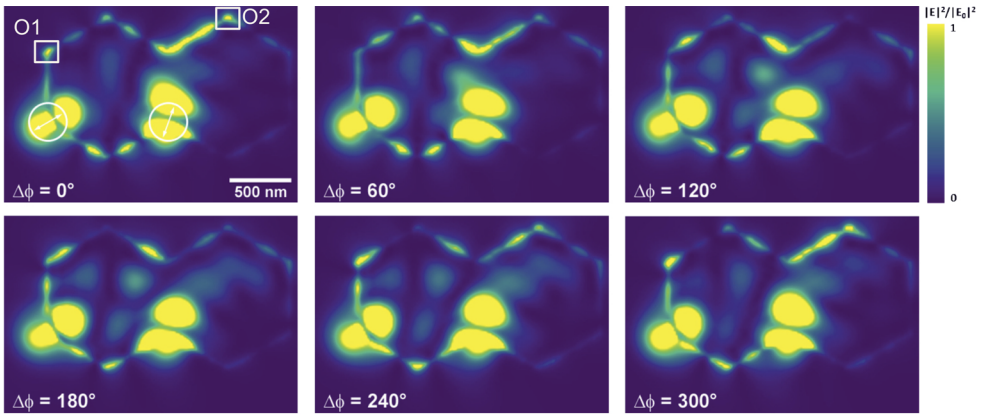

Fig. 7. Series of normalized near-field intensity maps calculated when entry nodes I_1 and I_2 are excited with a varying relative phase $\Delta\phi$ in I_2 with respect to I_1. The linear polarization of the incident fields is fixed, 30° for I_1 and 70° for I_2 (double arrows).

Optics EXPRESS

5. Conclusions

In this report, we have proposed two combined approaches to control the micrometer-scale spatial extension of nonlinear photoluminescence locally excited by ultrafast laser excitation and delocalized in an engineered crystalline plasmonic cavity. Such control is enabled by the manipulation of surface plasmon modes redistributing the excitation energy within the device. By favoring a subset of contributing modes through a polarization selection, we have demonstrated that regions of large nonlinear optical conversion can be readily re-configured. We have introduced a complementary strategy relying on the coherent build up of the surface plasmon landscape. The interference pattern of interacting surface plasmons is tuned by adjusting the phase difference between a pair of laser pulses impinging on the plasmonic cavity. This coherent superposition translates into a steerable spatial redistribution of the nonlinear photoluminescence emitted by the cavity.

Manipulating the spatial two-dimensional landscape of a nonlinear response brings new control strategies to develop plasmonic-based functional devices. For instance, it is the enabling mechanism to reconfigure arithmetic and Boolean operations or routing modalities recently reported in Ref. [48,50]. An additional central aspect brought by our results is the remarkable sensitivity of the nonlinear photoluminescence to the surface plasmon field. It opens innovative avenues for spatially controlling hot-carriers chemistry [51]. Since the nonlinear photoluminescence is likely to originate from an out-of-equilibrium electron distribution brought at elevated temperature by the pumped surface plasmon [43], our observation suggests that the electronic temperature can be locally adjusted across a two-dimensional micrometer-size plasmonic reactor.

Funding. Agence Nationale de la Recherche (ANR-15-IDEX-0003, ANR-17-EURE-0002, ANR-20-CE24-0001, ANR-21-ESRE-0040); European Regional Development Fund (FEDER-FSE Bourgogne 2014/2020); Conseil régional de Bourgogne-Franche-Comté; Centre National de la Recherche Scientifique.

Disclosures. The authors declare no conflicts of interest.

Data availability. Data underlying the results presented in this paper are not publicly available at this time but may be obtained from the authors upon reasonable request.

References

1. G. T. Boyd, Z. H. Yu, and Y. R. Shen, "Photoinduced luminescence from the noble metals and its enhancement on roughned surface," Phys. Rev. B **33**(12), 7923–7936 (1986).
2. P. J. Schuck, D. P. Fromm, A. Sundaramurthy, G. S. Kino, and W. E. Moerner, "Improving the mismatch between light and nanoscale objects with gold bowtie nanoantennas," Phys. Rev. Lett. **94**(1), 017402 (2005).
3. P. Ghenuche, S. Cherukulappurath, T. H. Taminiau, N. F. van Hulst, and R. Quidant, "Spectroscopic mode mapping of resonant plasmon nanoantennas," Phys. Rev. Lett. **101**(11), 116805 (2008).
4. E. Dulkeith, T. Niedereichholz, T. A. Klar, J. Feldmann, G. von Plessen, D. I. Gittins, K. S. Mayya, and F. Caruso, "Plasmon emission in photoexcited gold nanoparticles," Phys. Rev. B **70**(20), 205424 (2004).
5. A. Bouhelier, R. Bachelot, G. Lerondel, S. Kostcheev, P. Royer, and G. P. Wiederrecht, "Surface plasmon characteristics of tunable photoluminescence in single gold nanorods," Phys. Rev. Lett. **95**(26), 267405 (2005).
6. M. R. Beversluis, A. Bouhelier, and L. Novotny, "Continuum generation from single gold nanostructures through near-field mediated intraband transitions," Phys. Rev. B **68**(11), 115433 (2003).
7. K. Imura, T. Nagahara, and H. Okamoto, "Plasmon mode imaging of single gold nanorods," J. Am. Chem. Soc. **126**(40), 12730–12731 (2004).
8. P. Mühlschlegel, H.-J. Eisler, O. J. F. Martin, B. Hecht, and D. W. Pohl, "Resonant optical antennas," Science **308**(5728), 1607–1609 (2005).
9. R. Méjard, A. Verdy, M. Petit, A. Bouhelier, B. Cluzel, and O. Demichel, "Energy-Resolved Hot-Carrier Relaxation Dynamics in Monocrystalline Plasmonic Nanoantennas," ACS Photonics **3**(8), 1482–1488 (2016).
10. J. Chen, A. Krasavin, P. Ginzburg, A. V. Zayats, T. Pullerits, and K. J. Karki, "Evidence of high-order nonlinearities in supercontinuum white-light generation from a gold nanofilm," ACS Photonics **5**(5), 1927–1932 (2018).
11. M. Castro-Lopez, D. Brinks, R. Sapienza, and N. F. van Hulst, "Aluminum for nonlinear plasmonics: Resonance-driven polarized luminescence of al, ag, and au nanoantennas," Nano Lett. **11**(11), 4674–4678 (2011).
12. P. R. Wiecha, M.-M. Mennemanteuil, D. Khlopin, J. Martin, A. Arbouet, D. Gérard, A. Bouhelier, J. Plain, and A. Cuche, "Local field enhancement and thermoplasmonics in multimodal aluminum structures," Phys. Rev. B **96**(3), 035440 (2017).

Optics EXPRESS

13. K. Malchow and A. Bouhelier, "Photon bunching of the nonlinear photoluminescence emitted by plasmonics metals," J. Opt. Soc. Am. B **38**(2), 576 (2021).
14. J. Huang, W. Wang, C. J. Murphy, and D. G. Cahill, "Resonant secondary light emission from plasmonic Au nanostructures at high electron temperatures created by pulsed-laser excitation," Proc. Natl. Acad. Sci. **111**(3), 906–911 (2014).
15. J. T. Hugall and J. J. Baumberg, "Demonstrating Photoluminescence from Au is Electronic Inelastic Light Scattering of a Plasmonic Metal: The Origin of SERS Backgrounds," Nano Lett. **15**(4), 2600–2604 (2015).
16. T. Haug, P. Klemm, S. Bange, and J. M. Lupton, "Hot-Electron Intraband Luminescence from Single Hot Spots in Noble-Metal Nanoparticle Films," Phys. Rev. Lett. **115**(6), 067403 (2015).
17. L. Roloff, P. Klemm, I. Gronwald, R. Huber, J. M. Lupton, and S. Bange, "Light Emission from Gold Nanoparticles under Ultrafast Near-Infrared Excitation: Thermal Radiation, Inelastic Light Scattering, or Multiphoton Luminescence?" Nano Lett. **17**(12), 7914–7919 (2017).
18. N. dell Fatti and F. Vallée, "Ultrafast optical nonlinear properties of metal nanoparticles," Appl. Phys. B **73**(4), 383–390 (2001).
19. P. Ghenuche, S. Cherukulappurath, and R. Quidant, "Mode mapping of plasmonic stars using TPL microscopy," New J. Phys. **10**(10), 105013 (2008).
20. N. Verellen, D. Denkova, B. D. Clercq, A. V. Silhanek, M. Ameloot, P. V. Dorpe, and V. V. Moshchalkov, "Two-Photon Luminescence of Gold Nanorods Mediated by Higher Order Plasmon Modes," ACS Photonics **2**(3), 410–416 (2015).
21. G. Roubaud, S. Bidault, S. Gigan, and S. Grésillon, "Statistical nonlinear optical mapping of localized and delocalized plasmonic modes in disordered gold metasurfaces," ACS Photonics **8**(7), 1937–1943 (2021).
22. H. Wang, T. B. Huff, D. A. Zweifel, W. He, P. S. Low, and A. W. J.-X. Cheng, "In vitro and in vivo two-photon luminescence imaging of single gold nanorods," Proc. Natl. Acad. Sci. **102**(44), 15752–15756 (2005).
23. L. Tong, Q. Wei, A. Wei, and J.-X. Cheng, "Gold nanorods as contrast agents for biological imaging: Optical properties, surface conjugation and photothermal effects," Photochem. Photobiol. **85**(1), 21–32 (2009).
24. N. J. Durr, T. Larson, D. K. Smith, B. A. Korgel, K. Sokolov, and A. Ben-Yakar, "Two-photon luminescence imaging of cancer cells using molecularly targeted gold nanorods," Nano Lett. **7**(4), 941–945 (2007).
25. S. Viarbitskaya, O. Demichel, B. Cluzel, G. Colas des Francs, and A. Bouhelier, "Delocalization of Nonlinear Optical Responses in Plasmonic Nanoantennas," Phys. Rev. Lett. **115**(19), 197401 (2015).
26. A. Agreda, D. K. Sharma, S. Viarbitskaya, R. Hernandez, B. Cluzel, O. Demichel, J.-C. Weeber, G. Colas des Francs, G. P. Kumar, and A. Bouhelier, "Spatial Distribution of the Nonlinear Photoluminescence in Au Nanowires," ACS Photonics **6**(5), 1240–1247 (2019).
27. R. Hernandez, R. Juliano Martins, A. Agreda, M. Petit, J.-C. Weeber, A. Bouhelier, B. Cluzel, and O. Demichel, "Delocalized Hot Electron Generation with Propagative Surface Plasmon Polaritons," ACS Photonics **6**(6), 1500–1505 (2019).
28. D. K. Sharma, A. Agreda, J. Barthes, G. Colas des Francs, G. V. Pavan Kumar, and A. Bouhelier, "Wave-vector analysis of plasmon-assisted distributed nonlinear photoluminescence along Au nanowires," Phys. Rev. B **102**(11), 115414 (2020).
29. U. Kumar, S. Viarbitskaya, A. Cuche, C. Girard, S. Bolisetty, R. Mezzenga, G. Colas des Francs, A. Bouhelier, and E. Dujardin, "Designing Plasmonic Eigenstates for Optical Signal Transmission in Planar Channel Devices," ACS Photonics **5**(6), 2328–2335 (2018).
30. S. Grossmann, D. Friedrich, M. Karolak, R. Kullock, E. Krauss, M. Emmerling, G. Sangiovanni, and B. Hecht, "Nonclassical optical properties of mesoscopic gold," Phys. Rev. Lett. **122**(24), 246802 (2019).
31. S. Viarbitskaya, A. Teulle, A. Cuche, J. Sharma, C. Girard, E. Dujardin, and A. Arbouet, "Morphology-induced redistribution of surface plasmon modes in two-dimensional crystalline gold platelets," Appl. Phys. Lett. **103**(13), 131112 (2013).
32. S. Viarbitskaya, A. Teulle, R. Marty, J. Sharma, C. Girard, A. Arbouet, and E. Dujardin, "Tailoring and imaging the plasmonic local density of states in crystalline nanoprisms," Nat. Mater. **12**(5), 426–432 (2013).
33. A. Cuche, S. Viarbitskaya, J. Sharma, A. Arbouet, C. Girard, and E. Dujardin, "Modal engineering of Surface Plasmons in apertured Au Nanoprisms," Sci. Rep. **5**(1), 16635 (2015).
34. U. Kumar, A. Cuche, J. Sharma, A. Moreau, G. Colas des Francs, C. Girard, and E. Dujardin, "Spectral Tuning of High Order Plasmonic Resonances in Multimodal Film-Coupled Crystalline Cavities," Adv. Opt. Mater. **7**(11), 1801787 (2019).
35. J.-S. Huang, J. Kern, P. Geisler, P. Weinmann, M. Kamp, A. Forchel, P. Biagioni, and B. Hecht, "Mode Imaging and Selection in Strongly Coupled Nanoantennas," Nano Lett. **10**(6), 2105–2110 (2010).
36. M. Song, J. Dellinger, O. Demichel, M. Buret, G. Colas des Francs, D. Zhang, E. Dujardin, and A. Bouhelier, "Selective excitation of surface plasmon modes propagating in Ag nanowires," Opt. Express **25**(8), 9138 (2017).
37. H. Wei, Z. Li, X. Tian, Z. Wang, F. Cong, N. Liu, S. Zhang, P. Nordlander, N. J. Halas, and H. Xu, "Quantum Dot-Based Local Field Imaging Reveals Plasmon-Based Interferometric Logic in Silver Nanowire Networks," Nano Lett. **11**(2), 471–475 (2011).
38. G. Razinskas, D. Kilbane, P. Melchior, P. Geisler, E. Krauss, S. Mathias, B. Hecht, and M. Aeschlimann, "Normal-Incidence PEEM Imaging of Propagating Modes in a Plasmonic Nanocircuit," Nano Lett. **16**(11), 6832–6837 (2016).

Optics EXPRESS

39. R. Könenkamp, R. C. Word, J. P. S. Fitzgerald, A. Nadarajah, and S. D. Saliba, "Controlled spatial switching and routing of surface plasmons in designed single-crystalline gold nanostructures," Appl. Phys. Lett. **101**(14), 141114 (2012).
40. V. Remesh, M. Stührenberg, L. Saemisch, N. Accanto, and N. F. van Hulst, "Phase control of plasmon enhanced two-photon photoluminescence in resonant gold nanoantennas," Appl. Phys. Lett. **113**(21), 211101 (2018).
41. C. Rewitz, G. Razinskas, P. Geisler, E. Krauss, S. Goetz, M. Pawłowska, B. Hecht, and T. Brixner, "Coherent control of plasmon propagation in a nanocircuit," Phys. Rev. Appl. **1**(1), 014007 (2014).
42. P. Klemm, T. Haug, S. Bange, and J. M. Lupton, "Time-Domain Interferometry of Surface Plasmons at Nonlinear Continuum Hot Spots in Films of Silver Nanoparticles," Phys. Rev. Lett. **113**(26), 266805 (2014).
43. S. Viarbitskaya, A. Cuche, A. Teulle, J. Sharma, C. Girard, A. Arbouet, and E. Dujardin, "Plasmonic hot printing in gold nanoprisms," ACS Photonics **2**(6), 744–751 (2015).
44. J.-S. Huang, V. Callegari, P. Geisler, C. Brüning, J. Kern, J. C. Prangsma, X. Wu, T. Feichtner, J. Ziegler, P. Weinmann, M. Kamp, A. Forchel, P. Biagioni, U. Sennhauser, and B. Hecht, "Atomically flat single-crystalline gold nanostructures for plasmonic nanocircuitry," Nat. Commun. **1**(1), 150 (2010).
45. R. Méjard, A. Verdy, O. Demichel, M. Petit, L. Markey, F. Herbst, R. Chassagnon, G. Colas des Francs, B. Cluzel, and A. Bouhelier, "Advanced engineering of single-crystal gold nanoantennas," Opt. Mater. Express **7**(4), 1157–1168 (2017).
46. S. Boroviks, F. Todisco, N. A. Mortensen, and S. I. Bozhevolnyi, "Use of monocrystalline gold flakes for gap plasmon-based metasurfaces operating in the visible," Opt. Mater. Express **9**(11), 4209–4217 (2019).
47. Z. Guo, Y. Zhang, Y. DuanMu, L. Xu, S. Xie, and N. Gu, "Facile synthesis of micrometer-sized gold nanoplates through an aniline-assisted route in ethylene glycol solution," Colloids Surf., A **278**(1-3), 33–38 (2006).
48. U. Kumar, A. Cuche, C. Girard, S. Viarbitskaya, F. Dell'Ova, R. Al Rafrafin, G. Colas des Francs, S. Bolisetty, R. Mezzenga, A. Bouhelier, and E. Dujardin, "Interconnect-Free Multibit Arithmetic and Logic Unit in a Single Reconfigurable 3 μm ^{2} Plasmonic Cavity," ACS Nano **15**(8), 13351–13359 (2021).
49. A. V. Uskov, J. B. Khurgin, M. Buret, A. Bouhelier, I. V. Smetanin, and I. E. Protsenko, "Biased nanoscale contact as active element for electrically driven plasmonic nanoantenna," ACS Photonics **4**(6), 1501–1505 (2017).
50. A. Agreda, D. K. Sharma, G. Colas des Francs, G. V. P. Kumar, and A. Bouhelier, "Modal and wavelength conversions in plasmonic nanowires," Opt. Express **29**(10), 15366–15381 (2021).
51. S. Kumar, A. Habib, and R. Sundararaman, "Plasmonic hot carriers scratch the surface," Trends Chem. **3**(11), 902–910 (2021).